SI-ICAST2025

Journal of Intelligent Material Systems and Structures

Journal of Intelligent Material Systems and Structures
1–16

DOI: 10.1177/1045389X261445520
journals.sagepub.com/home/jim
Sage

Four-dimensional printed hierarchical mechanical metamaterials with piezoelectric sensing function integration

Haobo Wang[1], Xu Liu[2], Chengjun Zeng[1], Baoming Wang[3], Nan Li[1], Liwu Liu[1], Yanju Liu[1] and Jinsong Leng[4]

Abstract

This work presents a hierarchical 4D-printed mechanical metamaterial with reconfigurable, nonlinear mechanical behavior. An analytical framework is developed to predict its effective mechanical properties, demonstrating good agreement with finite-element simulations and experimental measurements. The metamaterial exhibits biomimetic, J-shaped stress-strain curves, indicating enhanced flexibility and compliance desirable for deployable structures. Moreover, the auxetic metamaterials achieve negative Poisson's ratios with high stretchability, thereby expanding the operational domain of metamaterials. Furthermore, these metamaterials are integrated with flexible piezoelectric electrodes to enable a self-sensing function. Experiments demonstrate that the proposed self-sensing metamaterials are capable of accurately sensing pressure signals while maintaining high flexibility and conformal contact. Owing to the thermally activated shape-memory effects of the metamaterial skeleton, the device allows reversible reconfiguration of mechanical and sensing responses under external stimuli. These results highlight the potential of self-sensing metamaterials for deployable space structures, morphing aircraft, and wearable electronics.

Keywords

mechanical metamaterials, 4D printing, piezoelectric, flexible sensor

Introduction

Across aerospace, aeronautics, implantable medical devices, and wearable systems, structural designs are expected to be lightweight, conformally compliant, deployable in situ, and reliable over long service lifetimes (Hong et al., 2017; Jeong et al., 2012; Kai et al., 2017; Rogers et al., 2010). However, conventional monolithic materials and traditional structural components seldom satisfy the multi-objective requirements of simultaneous load-bearing capacity, dynamic compliance, and state sensing (Benight et al., 2013; Chou et al., 2015; Sekitani and Someya, 2012; Wang et al., 2015b). Mechanical metamaterials, characterized by periodic microarchitectures and geometric parameter tunability, provide viable pathways to achieve unconventional mechanical responses and multifunctional, multiphysics coupling effects (Lu and Kim, 2014; Majidi, 2019; Markvicka et al., 2018). Furthermore, by integrating such architectures with intelligent materials, including self-sensing media and shape-memory polymers (Huang et al., 2022; Lin et al., 2014; Song et al., 2019; Su et al., 2016), programmable and self-sensing metamaterial systems can be developed to enable in-situ state identification and adaptive deployment under complex operating conditions (Fang et al., 2019; Feng et al., 2020; Li et al., 2025).

Chiral metamaterials are characterized by coupled rotational and axial deformation mechanisms. They

[1]Department of Astronautical Science and Mechanics, Harbin Institute of Technology (HIT), P. R. China
[2]Max Planck Institute for Intelligent Systems, Stuttgart, Germany
[3]Weihai Guangwei Composites Co. Ltd, P. R. China
[4]Center for Composite Materials and Structures, Harbin Institute of Technology (HIT), P. R. China

Corresponding authors:
Nan Li, Department of Astronautical Science and Mechanics, Harbin Institute of Technology (HIT), Harbin 150001, P. R. China.
Email: li_nan1221@hit.edu.cn

Liwu Liu, Department of Astronautical Science and Mechanics, Harbin Institute of Technology (HIT), Harbin 150001, P. R. China.
Email: liulw@hit.edu.cn

Data Availability Statement included at the end of the article

exhibit tunable nonlinear mechanical responses and can sustain relatively large deformations while displaying negative Poisson's ratio (NPR) behavior and J-shaped stress–strain characteristics. To further expand the design space and enhance extensibility and NPR performance, Hierarchical architectures inspired by fractal geometric subdivision have been incorporated into chiral systems. Fractal geometry describes structural configurations generated through recursive construction principles and scale-dependent geometric organization. Such hierarchical approaches increase the areal density of curved ligament members in two-dimensional layouts and improve conformability to complex surfaces (Overvelde et al., 2016; Zhai et al., 2021). Building on this concept, Wang et al. (2023) developed multilevel theoretical models for fractal metamaterials, demonstrating programmable mechanical responses and improved extensibility. Using recursive geometric construction, Meza et al. (2015) proposed hierarchical nanolattice metamaterials together with their analytical theory, demonstrating that yield strength and stiffness scale approximately with relative density in multi-level architectures. These three-dimensional hierarchical lattices exhibited advantageous structural characteristics, including high specific strength, tunable mass density, elevated bulk-to-shear modulus ratios, and negative Poisson's ratio behavior. The integration of architected metamaterials with flexible piezoelectric or piezoresistive materials has further enabled conformal pressure and strain sensing platforms (Li et al., 2024). Such systems have been explored in electrophysiological interfaces, precision monitoring devices, and radio-frequency components (Zhao et al., 2025). For example, fractal-based metamaterial substrates have been used to construct electromyography sensors with improved defect tolerance, and fractal-inspired electrode arrays have been developed for three-dimensional epicardial coverage (Xu et al., 2015). In addition to geometric design, additive manufacturing has played an important role in realizing such architected metamaterials. Techniques such as stereolithography and PolyJet printing have been widely adopted for fabricating chiral and hierarchical structures due to their high geometric resolution and potential for multi-material integration (Huang et al., 2016; Wang et al., 2015a). These capabilities have enabled the development of mechanically tunable metamaterial architectures with tailored deformation responses.

Despite these advances, in most reported self-sensing metamaterial systems, the mechanical and electrical properties remain fixed after fabrication. Consequently, key sensing parameters, such as sensitivity, dynamic range, and structural compliance, cannot be adaptively tuned to environmental variations or operational requirements. This constraint limits their applicability in scenarios requiring multi-condition adaptability, including wearable dynamic monitoring and thermally varying aerospace environments. To address this limitation, this study proposes a reconfigurable hierarchical hexa-chiral metamaterial, in which hierarchy is introduced through finite-order recursive subdivision of ligament segments within each representative unit cell while preserving the global periodic topology, and realizes integrated metamaterial–electrode fabrication with in-situ controllability via 4D printing. In this work, 4D printing refers to the thermo-responsive shape-memory-enabled reconfigurability of the printed metamaterial substrate. First, an analytical model is established to predict the effective modulus and Poisson's ratio of the hierarchical hexa-chiral metamaterials in the linear deformation regime, and these predictions are subsequently validated through finite-element simulations. The combination of hexa-chiral topology and recursive ligament-level hierarchy enhances structural extensibility and negative Poisson's ratio behavior. Furthermore, the shape-memory effect enables reversible tuning of the mechanical state of the metamaterial. On this basis, a flexible piezoelectric layer is integrated with the shape-memory metamaterial substrate to construct a reconfigurable pressure sensor that maintains mechanical compliance while achieving high sensitivity. Experimental results demonstrate that the introduction of the hierarchical metamaterial substrate improves the sensing performance of thin piezoelectric films under tensile and pressure loading. The resulting self-sensing system operates stably under diverse mechanical stimuli. Overall, this approach provides a systematic route toward predictive and reconfigurable mechano-electrical coupling in architected metamaterials.

Geometry and hierarchical architecture of the hexa-chiral metamaterial

The proposed metamaterial is constructed based on a hexa-chiral topology in which six curved ligaments are periodically arranged around circular nodes to form a representative unit cell, as illustrated in Figure 1. The global lattice remains strictly periodic, whereas structural hierarchy is introduced exclusively at the ligament level. As shown in Figure 1(a), a first-order ligament consists of a single curved beam segment characterized by its arc radius, central angle, thickness, and width. Higher-order architectures are generated through recursive subdivision of this primary arc. In the second-order configuration (Figure 1(b)), each ligament is composed of multiple interconnected curved beam segments with reduced geometric scale. Further refinement leads to higher-order hierarchical ligaments (Figure 1(c)), where geometric complexity increases while preserving the overall hexa-chiral connectivity of the unit cell. This recursive construction strategy enables systematic modulation of deformation mechanisms through ligament-level design, without altering the

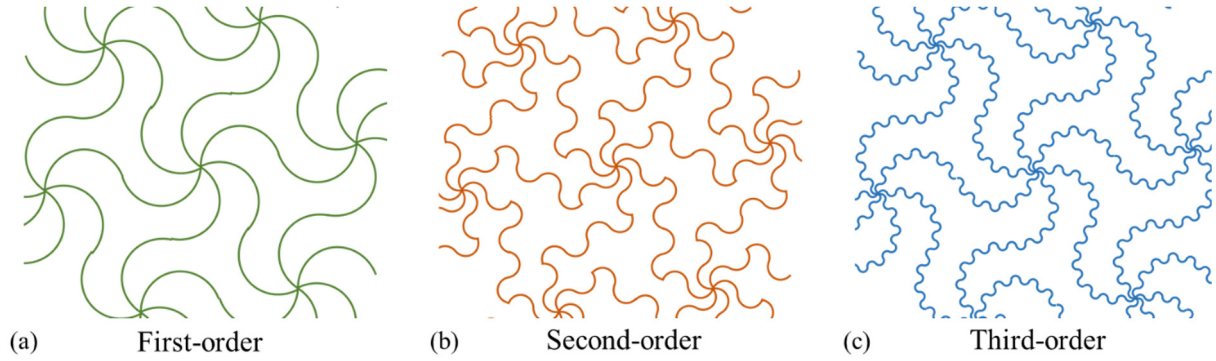

Figure 1. Geometry and hierarchical evolution of the hexa-chiral ligament architecture: (a) first-order ligament consisting of a single curved beam segment, (b) second-order hierarchical ligament obtained through recursive subdivision of the primary arc into multiple smaller curved segments while preserving global connectivity, and (c) higher-order hierarchical ligament with further geometric refinement at reduced scale.
The macroscopic periodic topology remains unchanged, whereas hierarchy is introduced solely at the ligament level, enabling modulation of deformation mechanisms without altering the global lattice arrangement.

macroscopic periodic arrangement. Consequently, stiffness, compliance, and auxetic response can be tuned through hierarchical architecture while maintaining identical global topology.

Analytical modeling of the hierarchical hexa-chiral metamaterial

To quantitatively link hierarchical ligament architecture with the macroscopic mechanical response of the periodic lattice, an analytical framework is established based on beam mechanics and structural energy equivalence. The formulation captures the contribution of ligament geometry and recursive hierarchical construction to the effective elastic modulus and Poisson's ratio of the representative unit cell. Through closed-form derivation, the model provides a parametric description of how ligament-level design governs the homogenized mechanical behavior of the hierarchical hexa-chiral metamaterial.

Throughout this section, consistent notation is adopted. Subscripts i = 1,2,3 refer to the ligaments within the representative unit cell, and superscripts A and B denote their two endpoints. The compliance matrix of an n-th-order ligament is written as (n), and the unit-cell stiffness matrix is denoted by D.

Mechanical model of first-order ligament

As shown in Figure 2(a), the first-order ligament is modeled as a curved beam segment that constitutes the fundamental deformable element of the hexa-chiral unit cell. Its geometry is defined by the arc radius, central angle, thickness, and width, which determine its axial and bending compliance. Based on beam mechanics and strain energy equivalence, the in-plane deformation of the curved ligament is formulated by considering coupled axial stretching and bending effects.

Under external uniaxial tension, each ligament can be simplified as a simply supported bending beam, as Figure 2(b). The loading on the ligament is reduced to an axial force N_0, bending moments M_A and M_B at both ends, and a shear force Q_0, where the shear force can be written as equation (1).

$$Q_0 = (M_A - M_B)/L_0 \tag{1}$$

The axial force $N(S)$ and bending moment $M(S)$at an arbitrary position along the neutral axis are expressed by equation (2), where $X'(S) = \mathrm{d}X(S)/\mathrm{d}S$ and $Y'(S) = \mathrm{d}Y(S)/\mathrm{d}S$.

$$\begin{cases} M(S) = M_A + N_0 Y(S) - Q_0 X(S) \\ N(S) = N_0 X'(S) + Q_0 Y'(S) \end{cases} \tag{2}$$

The total strain energy of a representative metamaterial unit containing ligaments of arbitrary shape is then given by equation (3), where S_0 is the total length of the ligament's neutral axis, E_s is the Young's modulus of the constituent material, and denote the axial and bending stiffnesses of the beam, respectively.

$$U = \frac{1}{2E_sA}\int_0^{S_0} N^2 \mathrm{d}S + \frac{1}{2E_sI}\int_0^{S_0} M^2 \mathrm{d}S \tag{3}$$

The total strain energy of a first-order ligament is obtained as equation (4).

$$\begin{aligned} U = {} & \frac{L_0}{2E_sA}(\beta_1 N_0^2 + \beta_2 N_0 (M_A - M_B)/L_0 \\ & + \beta_3 (M_A^2 + M_B^2 - 2M_A M_B)/L_0^2) \\ & + \frac{L_0}{2E_sI}[\beta_4 M_A^2 + \beta_5 (N_0 L_0)^2 + \beta_6 (M_A^2 + M_B^2 - 2M_A M_B) \\ & + \beta_7 M_A (N_0 L_0) + \beta_8 M_A (M_A - M_B) + \beta_9 (N_0 L_0)(M_A - M_B)] \end{aligned} \tag{4}$$

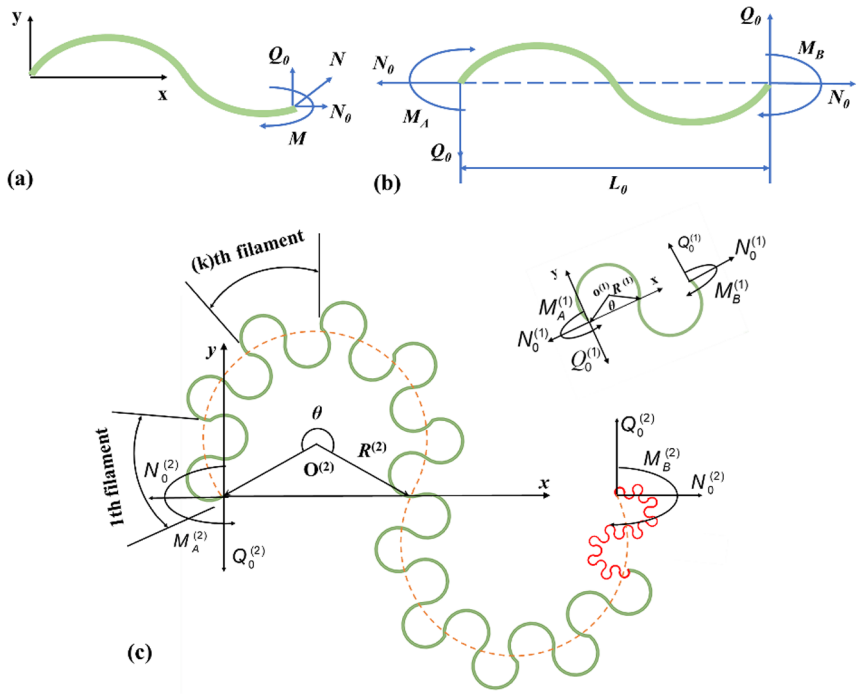

Figure 2. Graphic illustration of the first-order and the second-order ligament and their mechanical model: (a) the mechanical model of the first-order ligament in the Cartesian coordinate system *o-xy*, (b) the free-body mechanical model of the beam microstructure, and (c) the mechanical model of the second-order ligament.

By Castigliano's first theorem, the load–displacement relation and its dimensionless form for the ligament are derived as equation (5),

$$\begin{Bmatrix} \bar{u} \\ \omega_A \\ \omega_B \end{Bmatrix} = \begin{bmatrix} \frac{\bar{w}^2\beta_1}{12} + \beta_5 & \frac{\bar{w}^2\beta_2}{24} + \frac{1}{2}\beta_7 + \frac{1}{2}\beta_9 & -\frac{\bar{w}^2\beta_2}{24} - \frac{1}{2}\beta_9 \\ \frac{\bar{w}^2\beta_2}{24} + \frac{1}{2}\beta_7 + \frac{1}{2}\beta_9 & \frac{\bar{w}^2\beta_3}{12} + \beta_4 + \beta_6 + \beta_8 & -\frac{\bar{w}^2\beta_3}{12} - \beta_6 - \frac{1}{2}\beta_8 \\ -\frac{\bar{w}^2\beta_2}{24} - \frac{1}{2}\beta_9 & -\frac{\bar{w}^2\beta_3}{12} - \beta_6 - \frac{1}{2}\beta_8 & \frac{\bar{w}^2\beta_3}{12} + \beta_6 \end{bmatrix} \begin{Bmatrix} \bar{N}_0 \\ \bar{M}_A \\ \bar{M}_B \end{Bmatrix} \tag{5}$$

where βi ($i = 1,2, \ldots, 9$) are given as:

$$\beta_1 = \int_0^{S_0} [X'(S)]^2 \mathrm{d}S/L_0 = \csc(\theta/2)(\sin\theta + \theta)/4$$

$$\beta_2 = 2\int_0^{S_0} X'(S)Y'(S)dS/L_0^2 = 0$$

$$\beta_3 = \int_0^{S_0} [Y'(S)]^2 \mathrm{d}S/L_0 = \csc(\theta/2)(\theta - \sin\theta)/4$$

$$\beta_4 = S_0/L_0 = [\theta \csc(\theta/2)]/2$$

$$\beta_5 = \int_0^{S_0} [Y(S)]^2 dS/L_0^3 = \csc(\theta/2)[\csc^2(\theta/2)(\theta + \sin\theta) + 2\cot^2(\theta/2) - 4\sin\theta]/64$$

$$\beta_6 = \int_0^{S_0} [X(S)]^2 dS/L_0^3 = \csc(\theta/2)[10\theta + \theta\csc^2(\theta/2) - \csc(\theta/2)]/64$$

$$\beta_7 = 2\int_0^{S_0} Y(S)dS/L_0^2 = 0$$

$$\beta_8 = -2\int_0^{S_0} X(S)dS/L_0^2 = -\theta\csc(\theta/2)/2$$

$$\beta_9 = -2\int_0^{S_0} X(S)Y(S)dS/L_0^3 = \left(-\theta\cos\frac{\theta}{2} + 2\csc\frac{\theta}{2}\right)/16$$

The dimensionless width, displacement, force, and moment are defined in equation (6).

$$\bar{u} = \frac{u}{L_0}, \bar{w} = \frac{w}{L_0}, \bar{N}_0 = \frac{N_0 L_0^2}{E_s I}, \bar{Q}_0 = \frac{Q_0 L_0^2}{E_s I}, \quad \bar{M}_A = \frac{M_A L_0}{E_s I} \bar{M}_B = \frac{M_B L_0}{E_s I} \tag{6}$$

Mechanical model of n-order ligament microstructures

The hierarchical ligament configuration is illustrated in Figure 2(c). In this construction, a higher-order ligament is obtained through recursive subdivision of the first-order curved beam segment, resulting in a sequence of geometrically scaled ligament elements connected in series. For an n-order configuration, the ligament can be represented as a series assembly of 2^n first-order segments with reduced geometric scale while preserving overall connectivity.

Under the assumption of linear elastic deformation, the total strain energy of the hierarchical ligament is expressed as the sum of the strain energies stored in each first-order segment. The first-order microstructural stress–strain relation derived in equation (7) is therefore applied recursively to construct the effective compliance of the higher-order ligament.

$$\begin{pmatrix} \overline{u}^{(1)} \\ \overline{w_A}^{(1)} \\ \overline{w_B}^{(1)} \end{pmatrix} = \overline{\boldsymbol{T}}^{(1)} \begin{pmatrix} \overline{N_0}^{(1)} \\ \overline{M_A}^{(1)} \\ \overline{M_B}^{(1)} \end{pmatrix} \tag{7}$$

The expression for $\overline{T}^{(1)}$ can be found in Appendix 1. The total strain energy of the second-order ligament is given by equations (8) and (9), where $\boldsymbol{C}_k$ is a matrix determined by the ligament geometry.

$$\begin{aligned} W^{(2)} &= \sum_{k=1}^{2n} W_k^{(1)} \\ &= \frac{R^{(1)}}{2EI} \left(N_k^{(2)} R^{(2)}, M_{kA}^{(2)}, M_{kB}^{(2)}\right) \sum_{k=1}^{2n} \boldsymbol{C}_k^T \overline{\boldsymbol{T}}^{(1)} \boldsymbol{C}_k \\ &\quad \left(N_k^{(2)} R^{(2)}, M_{kA}^{(2)}, M_{kB}^{(2)}\right)^{\mathrm{T}} \end{aligned} \tag{8}$$

$$W^{(2)} = \frac{R^{(2)}}{2EI} \left(N^{(2)} R^{(2)}, M_A^{(2)}, M_B^{(2)}\right) \overline{\boldsymbol{T}}^{(2)} \left(N^{(2)} R^{(2)}, M_A^{(2)}, M_B^{(2)}\right)^{\mathrm{T}} \tag{9}$$

The expression for $\boldsymbol{C}_K$ can be found in Appendix 1. The compliance matrix of the second-order ligament $\overline{T}^{(2)}$ is then obtained from equations (10)–(12).

$$\overline{\boldsymbol{T}}^{(2)} = G \sum_{k=1}^{2n} \boldsymbol{C}_k^{\mathrm{T}} \overline{\boldsymbol{T}}^{(1)} \boldsymbol{C}_k \tag{10}$$

$$\left(\overline{T}_{11}^{(2)}, \overline{T}_{22}^{(2)}, \overline{T}_{33}^{(2)}, \overline{T}_{12}^{(2)}, \overline{T}_{13}^{(2)}, \overline{T}_{23}^{(2)}\right)^{\mathrm{T}} = \boldsymbol{D} \left(\overline{T}_{11}^{(1)}, \overline{T}_{22}^{(1)}, \overline{T}_{33}^{(1)}, \overline{T}_{12}^{(1)}, \overline{T}_{13}^{(1)}, \overline{T}_{23}^{(1)}\right)^{\mathrm{T}} \tag{11}$$

$$\left(\overline{T}_{11}^{(n)}, \overline{T}_{22}^{(n)}, \overline{T}_{33}^{(n)}, \overline{T}_{12}^{(n)}, \overline{T}_{13}^{(n)}, \overline{T}_{23}^{(n)}\right)^{\mathrm{T}} = \boldsymbol{D}^{n-1} \left(\overline{T}_{11}^{(1)}, \overline{T}_{22}^{(1)}, \overline{T}_{33}^{(1)}, \overline{T}_{12}^{(1)}, \overline{T}_{13}^{(1)}, \overline{T}_{23}^{(1)}\right)^{\mathrm{T}} \tag{12}$$

By recursion, the compliance matrix of an n-order ligament structure follows equation (13), where the compliance matrix $\boldsymbol{D}$ depends only on the central angle of the circular arc and the number of first-order microstructures (see equation (23), Appendix 2).

$$\left(\overline{T}_{11}^{(2)}, \overline{T}_{22}^{(2)}, \overline{T}_{33}^{(2)}, \overline{T}_{12}^{(2)}, \overline{T}_{13}^{(2)}, \overline{T}_{23}^{(2)}\right)^{\mathrm{T}} = \left(\lim_{m \to +\infty} \boldsymbol{D}^{n-1}\right) \left(\overline{T}_{11}^{(1)}, \overline{T}_{22}^{(1)}, \overline{T}_{33}^{(1)}, \overline{T}_{12}^{(1)}, \overline{T}_{13}^{(1)}, \overline{T}_{23}^{(1)}\right)^{\mathrm{T}} \tag{13}$$

Mechanical model of multilevel metamaterials

To establish the mechanical model of a fractal-inspired hexa-chiral metamaterial, the static equilibrium and kinematic compatibility equations are combined with the above load–displacement relations. Figure 3(a) to (c) showed the metamaterial under a uniform longitudinal tensile load and its representative unit cell containing three ligaments. The free-body diagrams of the ligaments in the unit cell are given in Figure 2(d) and (e). The three ligaments are labeled "1" "2" and "3"; their axial forces, shear forces, and bending moments are denoted by N_i, Q_i, M_{iA}, and M_{iB} (i = 1,2,3), respectively. The external equilibrium of the unit cell along 0° and the internal nodal equilibrium follow equation (24) in Appendix 3, yielding the static equilibrium conditions summarized in equation (25). Based on deformation compatibility, the relationships among deformation components are given by equation (26). Under the small-deformation assumption, the unit-cell compatibility reduces to equation (27). The effective strain of the network materials is defined as the percentage of elongation along the horizontal direction, as given by:

$$\varepsilon_x = u_1 \tag{14}$$

The dimensionless ligament load–displacement relations can be written as equation (15), where the entries of matrix $\mathbf{T}$ are β_i (i = 1,2,…,7,8).

$$\begin{Bmatrix} \overline{u} \\ \omega_A \\ \omega_B \end{Bmatrix} = \left[\overline{\boldsymbol{T}}\right] \begin{Bmatrix} \overline{N}_0 \\ \overline{M}_A \\ \overline{M}_B \end{Bmatrix} = \begin{bmatrix} \mathrm{t}_{11} & t_{12} & t_{13} \\ t_{12} & t_{22} & t_{23} \\ t_{13} & t_{23} & t_{33} \end{bmatrix} \begin{Bmatrix} \overline{N}_0 \\ \overline{M}_A \\ \overline{M}_B \end{Bmatrix} \tag{15}$$

By incorporating the equilibrium conditions specific to the hexa-chiral unit cell and the recursive compliance relations of the hierarchical ligaments, the coupled load–displacement response of the three independent

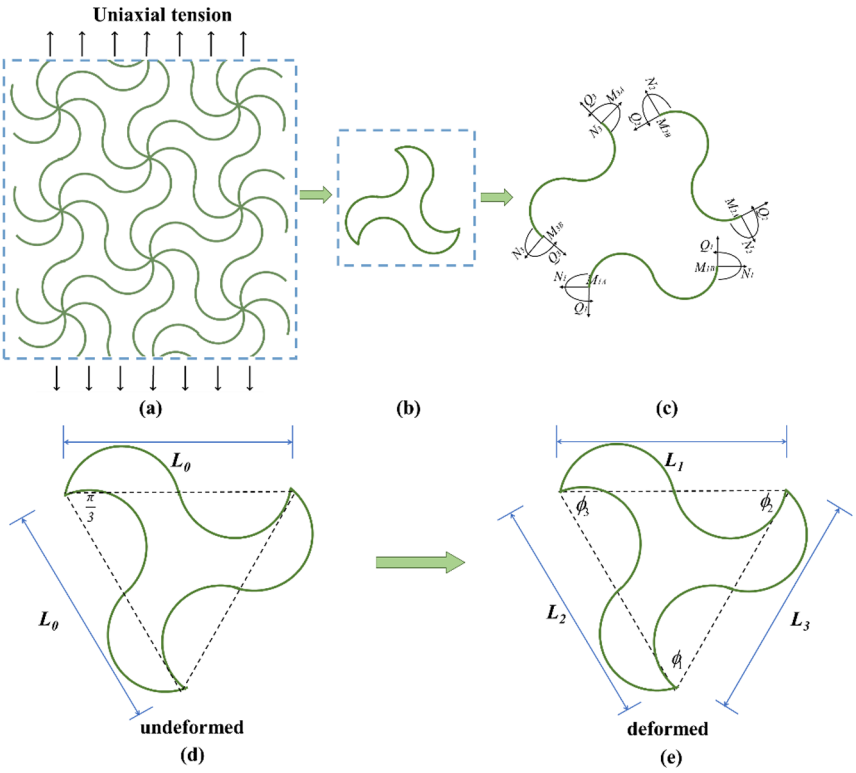

Figure 3. Schematic diagrams of the mechanical and deformation models of the representative unit of the auxetic metamaterial: (a) a tetra auxetic metamaterial that is subjected to uniaxial tensile stress along the perpendicular direction, (b) a representative unit of the tetra auxetic metamaterial, (c) the free-body diagram of six ligaments in a representative unit, (d) undeformed representative unit, and (e) deformed representative unit.

ligaments can be expressed in the compact matrix form of equation (16).

$$\begin{bmatrix} \overline{u}_1 & \overline{u}_2 & \overline{u}_3 \\ \omega_{1A} & \omega_{2A} & \omega_{3A} \\ \omega_{1B} & \omega_{2B} & \omega_{3B} \end{bmatrix} = \begin{bmatrix} t_{11} & t_{12} & t_{13} \\ t_{12} & t_{22} & t_{23} \\ t_{13} & t_{23} & t_{33} \end{bmatrix} \begin{bmatrix} \overline{N}_1 & \overline{N}_2 & \overline{N}_3 \\ \overline{M}_{1A} & \overline{M}_{2A} & \overline{M}_{3A} \\ \overline{M}_{1B} & \overline{M}_{2B} & \overline{M}_{3B} \end{bmatrix} \tag{16}$$

Substituting the ligament-level compliance into the unit-cell equilibrium equations yields the global load–displacement relation of the hexa-chiral unit cell, as given in equation (17).

$$\begin{bmatrix} \bar{N}_1 & \bar{N}_2 & \bar{N}_3 \\ \bar{M}_{1A} & \bar{M}_{2A} & \bar{M}_{3A} \\ \bar{M}_{1B} & \bar{M}_{2B} & \bar{M}_{3B} \end{bmatrix} = \begin{bmatrix} d_{11} & d_{12} & d_{13} \\ d_{12} & d_{22} & d_{23} \\ d_{13} & d_{23} & d_{33} \end{bmatrix} \begin{bmatrix} \bar{u}_1 & \bar{u}_2 & \bar{u}_3 \\ \omega_{1A} & \omega_{2A} & \omega_{3A} \\ \omega_{1B} & \omega_{2B} & \omega_{3B} \end{bmatrix} \tag{17}$$

An analytic solution to the elastic modulus of the material is obtained as:

$$E = \frac{2\sqrt{3}(d_{11} + d_{22} - 2d_{23} + d_{33})\left[-(d_{12} - d_{13})^2 + d_{11}(d_{22} - 2d_{23} + d_{33})\right]E_S I\bar{w}}{\left[-2(d_{12} - d_{13})^2 + (d_{22} - 2d_{23} + d_{33})(3d_{11} + d_{22} - 2d_{23} + d_{33})\right]AL_0^2} \tag{18}$$

According to the geometric relation, the transverse strain of the triangular hexachiral materials can be given by:

$$\varepsilon_y = \frac{2\bar{u}_2 + 2\bar{u}_3 - \bar{u}_1}{3} = \bar{u}_3 + \frac{\omega_{1B} - \omega_{3B}}{\sqrt{3}} \tag{19}$$

Then, the linear Poisson's ratio (v) of the hexa-chiral materials can be determined as:

$$\nu = -\frac{\varepsilon_y}{\varepsilon_x} = \frac{2(d_{12} - d_{13})^2 - (d_{11} - d_{22} + 2d_{23} - d_{33})(d_{22} - 2d_{23} + d_{33})}{2(d_{12} - d_{13})^2 - (d_{22} - 2d_{23} + d_{33})(3d_{11} + d_{22} - 2d_{23} + d_{33})} \tag{20}$$

The analytical framework developed in this section establishes a direct link between hierarchical ligament geometry and the effective mechanical response of the hexa-chiral metamaterial. By recursively constructing the compliance of higher-order fractal ligaments and embedding it into the unit-cell equilibrium and compatibility relations, the model yields closed-form expressions for the effective elastic modulus and Poisson's ratio in the small-deformation regime. With geometric parameters as inputs, the formulation provides an efficient means to evaluate the stiffness characteristics of the lattice and to capture the underlying structure–property relationships associated with hierarchical geometry. This analytical description serves as a useful basis for interpreting the mechanical behavior of the system, and its predictions are further examined through comparison with finite-element simulations in the following section.

Nonlinear mechanical response of the metamaterial

This section investigates the nonlinear mechanical response of the hierarchical mechanical metamaterial under uniaxial tension. To systematically validate the theoretical framework established in Section 3, the analytical predictions of the stress–strain behavior are comprehensively compared with both finite-element analysis (FEA) and direct experimental measurements based on the constituent material's characterization. Furthermore, the thermally activated shape-memory behavior of the 3D-printed PLA skeleton is evaluated, establishing the physical basis for the 4D reconfigurable sensing capabilities demonstrated in the subsequent sections.

Finite-element model setup and constituent material parameters

Finite-element analyses were performed using the commercial software Abaqus (Dassault Systèmes). The hexa-chiral unit-cell geometry was generated by parameterized Python scripts that automatically build both first- and second-order hierarchical structures for arbitrary central angle θ, ligament width w, and hierarchical order n, export the geometry to Abaqus CAE, apply boundary conditions, run the analysis, and extract force–displacement histories.

Following established practice for planar lattice structures of this type (Li et al., 2023), the metamaterial ligaments were discretized using two-node Timoshenko beam elements (B21 in Abaqus). The element size was set to w/5 along each ligament, and a mesh convergence check confirmed that the force–displacement response changed by less than 1% upon halving the element size. Periodic boundary conditions were imposed at the left and right boundaries of the unit cell to replicate infinite-lattice behavior: equal horizontal displacements were enforced at corresponding node pairs on the lateral edges. A prescribed displacement was applied to the top reference node along the loading direction, while the bottom reference node was fully fixed. Effective stress and strain were computed from the reaction force and applied displacement normalized by the unit-cell cross-sectional area and height, respectively. The constituent material is PLA, characterized through standard uniaxial tensile and stress-relaxation experiments on printed specimens (ASTM D638; Zwick-010 tensile tester with environmental chamber; tensile speed 2 mm min^{-1}). At room temperature (25°C), the measured Young's modulus, tensile strength, and failure strain of the printed PLA are $E_s = 1.6$ GPa, $\sigma_y = 50$ MPa, and $\delta = 10\%$, respectively.

Comparison of analytical predictions and finite-element results

Based on the closed-form expressions derived in Section 3, a fully analytical solver was constructed to evaluate the effective elastic response of the hierarchical hexa-chiral lattice. For each prescribed geometric configuration, the compliance components d_{ij} were first obtained from the unit-cell formulation, and the effective modulus E_{eff} was subsequently computed using equation (18). In the small-deformation regime, the macroscopic response was reconstructed as a linear stress–strain relation, $\sigma = E_{\text{eff}}\varepsilon$, enabling direct comparison with finite-element simulations. To ensure strict geometric consistency between theory and FEM, identical unit-cell parameters were employed in both models, including ligament span L_0, central angle θ, ligament width parameter w, beam cross-section (1×1 mm^2), and overall specimen dimensions. The hierarchical level was implemented consistently by subdividing each ligament segment analytically (via parameter n) and geometrically in the FEM model through the same recursive construction logic. This alignment guarantees that any discrepancy arises from modeling assumptions rather than geometric mismatch.

Finite-element simulations were performed using beam elements under displacement-controlled uniaxial loading, following the same boundary conditions assumed in the analytical formulation. The reaction force was normalized by the nominal cross-sectional area to obtain macroscopic stress, while strain was defined as the applied displacement divided by specimen height. All post-processing steps were automated to eliminate subjective data handling. As shown in Figure 4(b) and (d), the analytical predictions agree well with FEM results for both first-order and second-order architectures within the small-strain linear

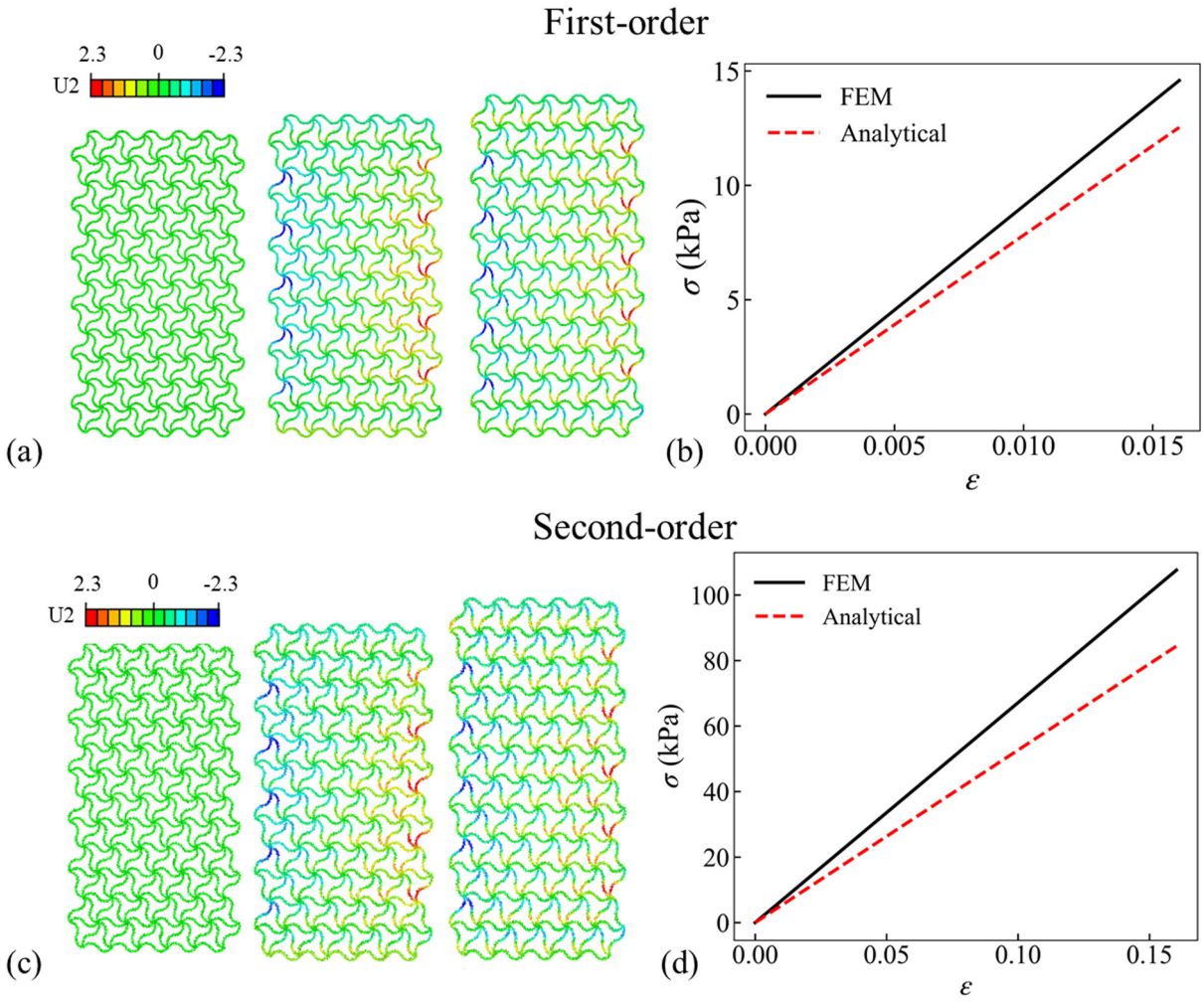

Figure 4. Deformation fields and stress–strain comparison of hierarchical hexa-chiral metamaterials under uniaxial tension in the 0° loading direction: (a) first-order structure: displacement contours (U_2) at increasing strain levels showing auxetic lateral expansion, (b) corresponding stress–strain curves comparing finite-element simulation (solid line) and analytical prediction (dashed line), (c) second-order hierarchical structure: displacement contours (U_2) illustrating enhanced rotational deformation and lateral expansion, and (d) stress–strain comparison between FEM and analytical results for the second-order structure.
The analytical model captures the overall stiffness trend and magnitude in the small-deformation regime, while minor deviations arise from shear deformation and geometric nonlinear effects included in FEM.

regime. The theoretical curves slightly underestimate the stiffness compared with FEM, which can be attributed to idealized Euler–Bernoulli bending assumptions in the analytical derivation, whereas the finite-element model inherently accounts for finite ligament thickness and shear effects. Nevertheless, the proportional scaling of stiffness between hierarchical levels is accurately captured.

In addition to the stress–strain comparison, displacement contour fields generated automatically for both first- and second-order structures (Figure 4(a) and (c)) further validate the mechanical consistency of the models. The plotted U_2 displacement fields clearly exhibit lateral expansion under axial tensile loading, confirming the auxetic behavior of the hexa-chiral lattice. The second-order hierarchical structure displays amplified transverse deformation relative to the first-order case, consistent with the increased compliance predicted analytically. The agreement between analytical stiffness scaling, FEM stress–strain response, and transverse displacement patterns demonstrates that the proposed theoretical framework reliably captures both the effective elastic modulus and the auxetic deformation mechanism of hierarchical six-ligament lattices. While the analytical model captures the overall stiffness trend and provides a reasonable approximation in the initial deformation stage, it is derived based on the symmetric reference configuration and simplified beam assumptions. As deformation progresses or when the geometry is altered through shape programming, the ligament configuration evolves and local symmetry is no longer strictly preserved. In such cases, the mechanical

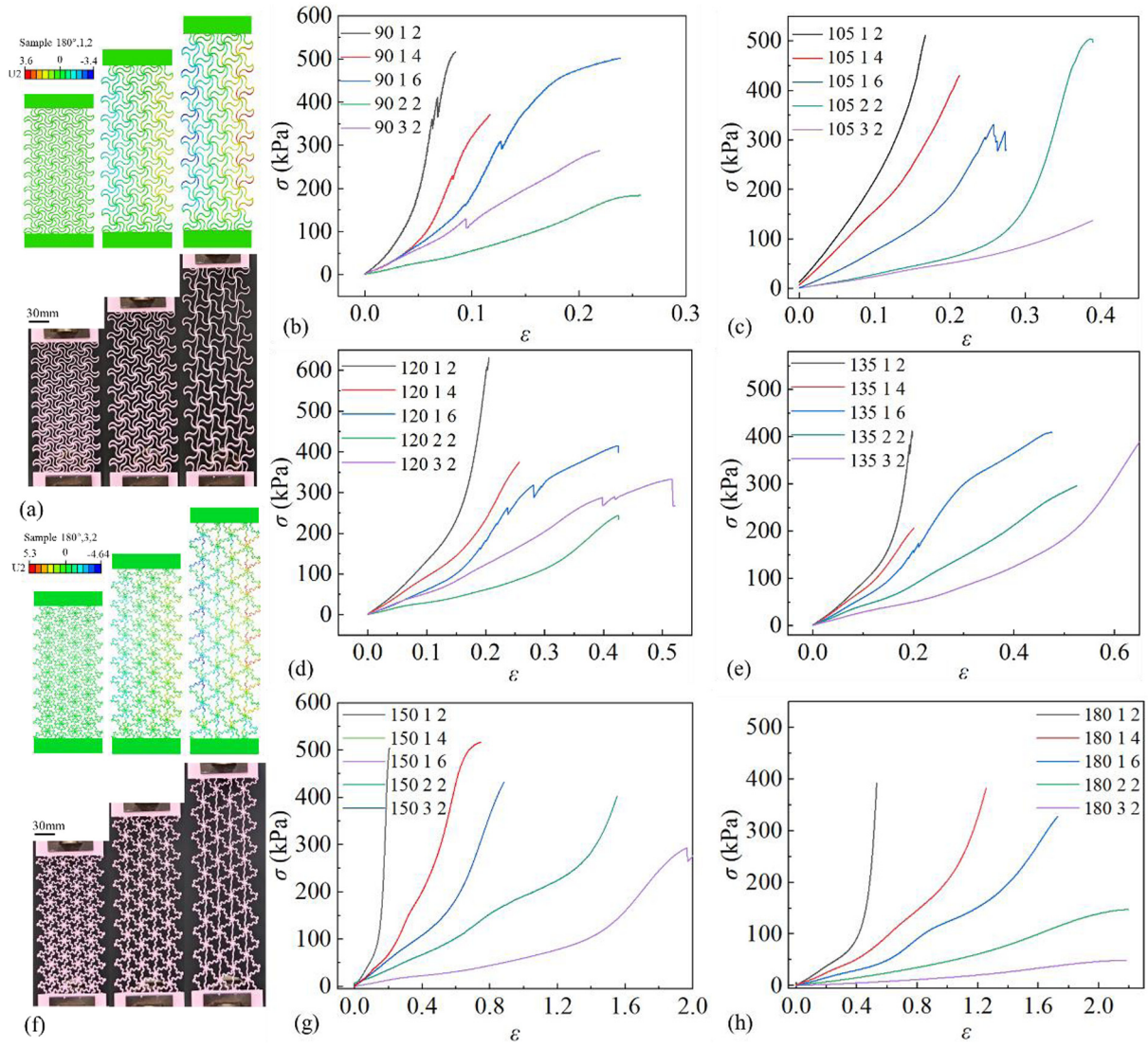

Figure 5. Experiment and FEA results of stress-strain curves: (a) the comparison of optical images and FEM results under different ε, (b)–(e) σ-λ curves in 0° direction of the first-order and second-order structures with n = 246, and (f)–(h) σ-λ curves of the first-order and second-order structures with n = 246.

response is more accurately captured by finite-element simulations, which naturally account for geometric evolution and nonlinear deformation effects.

Finite-element and experimental validation

This section investigates the nonlinear mechanical response of a fractal-geometry-inspired hexa-chiral mechanical metamaterial under uniaxial tension in the representative 0° direction. We first performed finite-element analysis (FEA) and mechanical testing on the constituent continuous material used for printing. Uniaxial tensile tests were conducted under displacement-controlled loading using symmetric gripping conditions to minimize boundary-induced bending effects, and at least three specimens were tested for each configuration to ensure repeatability. Under uniaxial tensile loading, both first- and second-order hexa-chiral metamaterials exhibit pronounced nonlinear behavior. The variations of Poisson's ratio ν and the effective modulus (E/E_S) evolve with the deformation mode. Poisson's ratio was calculated as the negative ratio of averaged transverse strain to axial strain in the small-to-moderate deformation regime, and the reported values correspond to the mean response of repeated samples. These unusual mechanical responses originate from the geometric design and the topological arrangement of filamentary microstructures within the unit cells.

Experimental and FEA results, together with the measured stress–strain σ-ε curves in the 0° direction. As seen in Figure 5(a), the initially curved ligaments gradually straighten as λ increases; the ligaments first

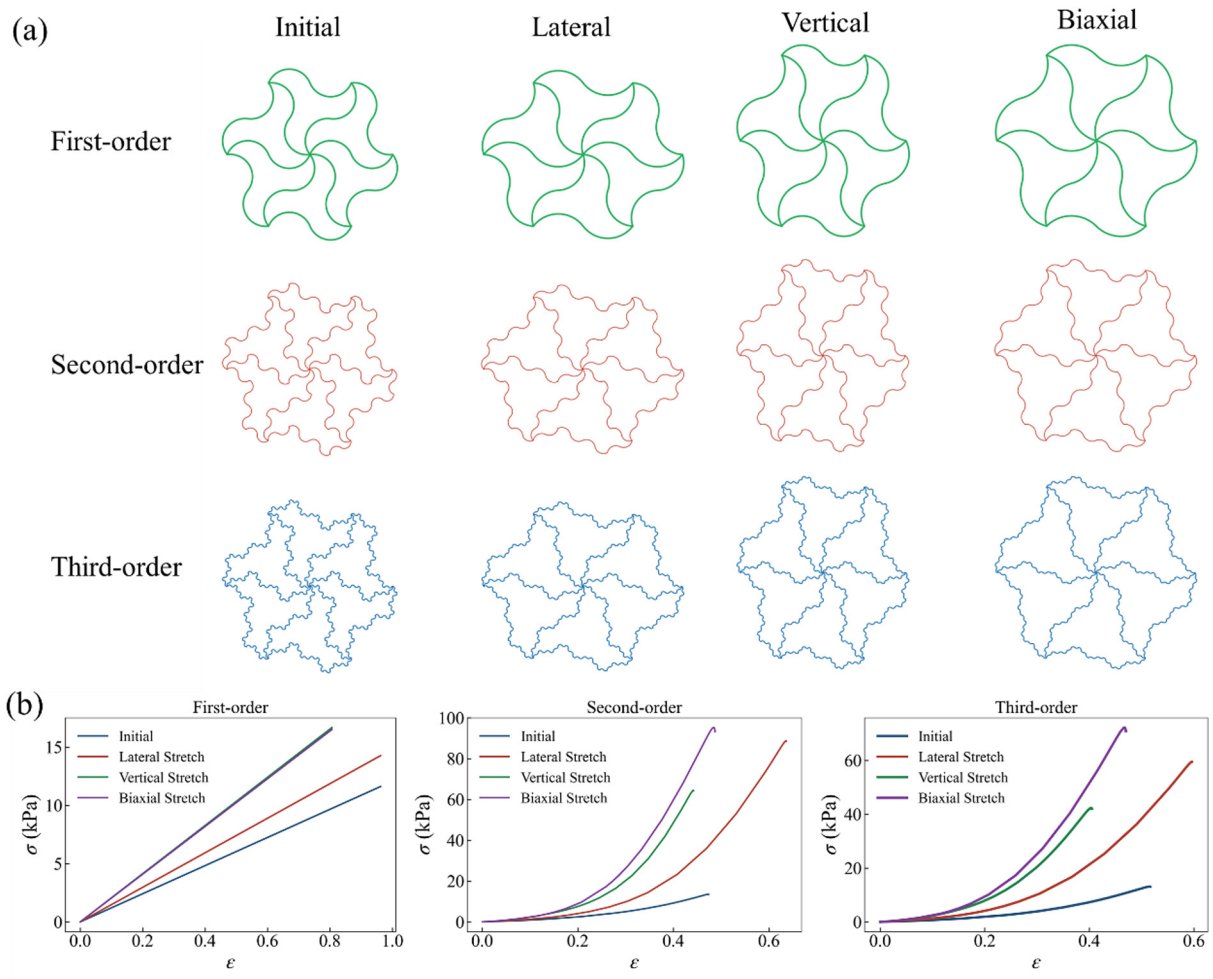

Figure 6. Shape-memory-enabled geometric reconfiguration and mechanically tunable response of hierarchical hexa-chiral metamaterials: (a) geometric evolution of first-, second-, and third-order unit cells under thermo-induced programming, showing multiple reconfigured states with different ligament curvatures while preserving the overall topology and (b) finite-element simulated stress–strain responses under different loading conditions (initial, lateral, vertical, and biaxial stretching), demonstrating the influence of geometric reconfiguration and hierarchical order on stiffness and nonlinear behavior.

undergo bending-dominated deformation and then plastic deformation, yielding nonlinear behavior in both first- and second-order structures. Figure 5(b) to (e) provides the σ-ε curves under uniaxial tension at 0° for first-order metamaterials with different geometric parameters. The FEA results are superimposed on the experimental curves as solid lines; the two agree closely across the full strain range tested, with a maximum point-wise deviation below 12%. In the small-deformation regime, this is consistent with the analytical–FEA agreement established in Section 4.2. At larger strains, FEA captures the geometric nonlinearity and onset of ligament plastic yielding that lie outside the scope of the closed-form model.

At small strains $\varepsilon < \varepsilon_{cr}$, the response is bending-dominated: the curved ligaments progressively unfold with increasing ε. In this stage, the σ-ε curve rises modestly, reflecting a relatively low effective modulus (E_1/E_S). As the curved ligaments are straightened, the response exhibits a markedly accelerated increase; when the strain surpasses the transition strain ε_{tr} and further exceeds ε_{cr}, the structure enters a stretch-dominated regime. Because bending compliance is lost in both first- and second-order architectures, the effective modulus increases sharply, producing a characteristic J-shaped σ-ε curve.

The programmable reconfiguration capability of the hierarchical hexa-chiral metamaterial is illustrated in Figure 6. A representative unit cell with prescribed geometry is selected as the reference configuration, corresponding to the initially printed state. Owing to the thermo-responsive shape-memory behavior of the PLA skeleton, the same structure can be reconfigured into multiple geometric states without re-fabrication, as shown in Figure 6(a). During reconfiguration, the horseshoe ligaments undergo geometric evolution,

resulting in variations in ligament curvature while preserving the global hexa-chiral topology. These reconfigured states correspond to distinct geometric configurations derived from the same initial unit cell and represent different mechanically programed states. The corresponding mechanical responses, obtained from finite-element simulations, are presented in Figure 6(b). Different reconfigured states exhibit clearly distinguishable stress–strain behaviors. As the ligament geometry evolves from a more curved to a less curved configuration, the deformation mechanism transitions from bending-dominated to stretching-dominated, leading to systematic variations in stiffness and nonlinear response. It is noted that the analytical model is established for the symmetric reference configuration and primarily captures the response in the small-deformation regime. For the reconfigured states shown in Figure 6, the mechanical behavior is therefore evaluated mainly through finite-element simulations. These results demonstrate that a single printed metamaterial can switch among multiple mechanical states through thermo-induced geometric reconfiguration, enabling post-fabrication tuning of mechanical and sensing performance.

Integration of self-sensing via piezoelectric materials

Flexible sensors are attractive for their high sensitivity and conformal, dynamic compliance; however, existing studies remain constrained by structure design, material selection, and fabrication routes. In this chapter, we integrate fractal mechanical metamaterials with bio-inspired flexible micro/nanostructures to fabricate a thermally responsive, reconfigurable flexible pressure sensor. The design expands both sensitivity and dynamic range, while overcoming the common limitation that device performance cannot be adjusted post-fabrication to match varying environments and usage requirements.

Fabrication of the metamaterial-based electronic skin features a multilayered structure, which is assembled into an integral device after each layer is fabricated separately. The fabrication processes of the main structural components are as follows. All metamaterial skeletal structures were modeled using the 3D modeling software SolidWorks to achieve smooth variations in filament curvature. All experimental specimens were produced using an FDM 3D printer (Bambu Lab, X1 Carbon) with PLA printing filament. A photograph of the fabricated multiscale metamaterial structure is shown in Figure 7(a). The 4D-printed framework was fabricated using a FDM printer equipped with a 0.2 mm nozzle. Considering the nozzle diameter and printer motion precision ($\sim$0.1 mm), the minimum reliably printed ligament thickness and width were approximately 0.4 mm (400 μm). The printed hierarchical lattice exhibits a negative Poisson's ratio effect, as evidenced by the lateral expansion under axial stretching, enabling effective conformal adaptation to dynamically moving skin surfaces.

After obtaining the above key components, the piezoelectric composite film was prepared, and the flexible electronic skin was assembled according to the following procedure, as illustrated in Figure 7(b) to (f). First, Ecoflex Parts A and B were mixed at a 1:1 ratio, and then a mixed powder of P(VDF-TrFE) and $BaTiO_3$ with graded volume fractions was added to the Ecoflex mixture. The solution and powders were thoroughly stirred to mix, after which the mixed solution was left to stand for defoaming. A uniform electro-receptive film was obtained using a 0.2 mm-thick film applicator, and the film was then cured at room temperature for later use. The electro-receptive film was subsequently subjected to thermal charging treatment (thermal poling). Next, a series of multiscale metamaterial structures with a thickness of 0.2 mm was fabricated using an FDM 3D printer and PLA filament. Using PDMS, the above film and the 4D-printed metamaterial were assembled into an integrated structure and placed into a pre-prepared encapsulation mold. Conductive silver paste was coated on both sides of the film, and lead wires were fixed on each side. The Ecoflex mixture prepared in step 1, together with the stacked assembly fixed on an acrylic plate, was introduced into the 3D-printed mold, and a 0.4 mm-thick film applicator was used to obtain uniform encapsulation. Finally, the material was cured at room temperature, and the encapsulated self-sensing metamaterial structure was removed from the mold.

Electrical characterization of the flexible sensor

The assembled metamaterial piezoelectric sensor is shown in Figure 8(a). The displayed periodic lattice corresponds to the macroscopic assembly of hierarchical hexa-chiral unit cells, whereas the structural hierarchy is embedded within the ligament architecture of each unit cell. The NPR effect of the metamaterial substrate endowed the flexible sensor with auxetic properties, generating lateral expansion while longitudinally stretching, which can better fit dynamic human skin and joints. The negative Poisson's ratio behavior was verified by both finite-element simulations and tensile experiments, where the transverse strain was directly measured and confirmed to be positive under axial tension, indicating auxetic expansion ($\nu < 0$). The measured Poisson's ratio remained negative within the operational strain range of the sensor. The self-sensing characteristics of the piezoelectric sensors were analyzed in this section. The output signals were obtained

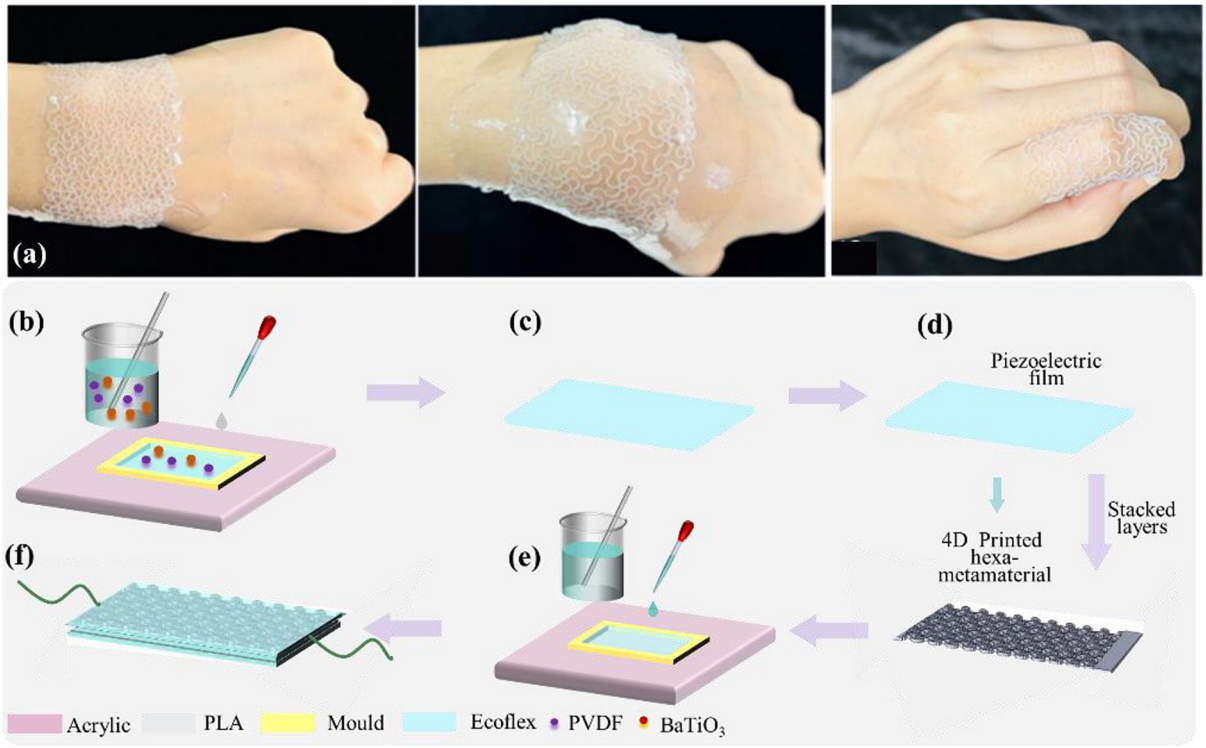

Figure 7. The manufacturing process of the flexible sensor: (a) dynamic conformity of the as-fabricated 4D printed metamaterials, (b)–(d) The fabrication process of piezoelectric film, and (e) and (f) assemble process of self-sensing metamaterial.

under gradient-pressure and gradient-frequency loads with self-built electromechanical experimental device. Unless otherwise specified, all electrical measurements were conducted on $n = 5$ independently fabricated sensor samples, and the reported results represent the averaged response. The variation between samples was within an acceptable experimental range, indicating good fabrication repeatability. When uniform loads with a fixed frequency was applied to the self-sensing sensor with gradient pressure from 5 to 20 kPa, the open-circuit voltage (Voc) was obtained as shown in Figure 8(b). In addition, the response characteristics of flexible metamaterial sensors to pressure signals of different frequencies were evaluated through tests, as shown in Figure 8(c). The output signal exhibited good linearity as the pressure increased. Further, the average short-circuit current of metamaterial sensors with gradient piezoelectric particles under external loading is shown in Figure 8(d). It can be seen that, under the same pressure, the short-circuit current of the sensors increased with the particle volume fraction in the electrodes. As the ultimate pressure increases, the signal rises in a stepwise manner as shown in Figure 8(e). In addition, the durability and stability of the flexible sensor were evaluated, as shown in Figure 8(f). Tensile cycling tests with a frequency of 1 Hz and a pressure of 5 kPa were employed. It can be observed that, during steady loading, the signal exhibits high stability.

The sensing function of the self-sensing metamaterial was demonstrated through multi-scenario real-time information acquisition, as shown in Figure 9. To verify its ability to monitor joint-motion signals, the metamaterials were attached to the finger joint and wrist, as shown in Figure 9(a) and (b). First, the sensor was placed on the second knuckle of the index finger for testing. The finger joint was bent inward sequentially to 0°, 30°, 60°, and 90°, each angle being held steady for several seconds, and then returned from 90° to 0° in sequence to complete one test cycle. Each cycle was repeated four times. The gage factor (GF) was calculated from the relative resistance variation ($\Delta R/R_0$) with respect to applied strain within the working deformation range. Although the curves exhibit some jitter—possibly influenced by finger tremor and bending speed—all metamaterials can distinguish the gradient bending angles of the finger joint through the peak features of the signal. Motion tests for the wrist were obtained using the same method. Furthermore, an experimental setup was used to compare the responses of the self-sensing metamaterials and a commercial sensor to irregular signals generated by falling droplets, and the results showed good consistency between the two, as shown in Figure 9(c). The pressure sensitivity was defined as the slope of the output signal with respect to applied pressure within the operating pressure range. Finally, passive sensing of human pulse

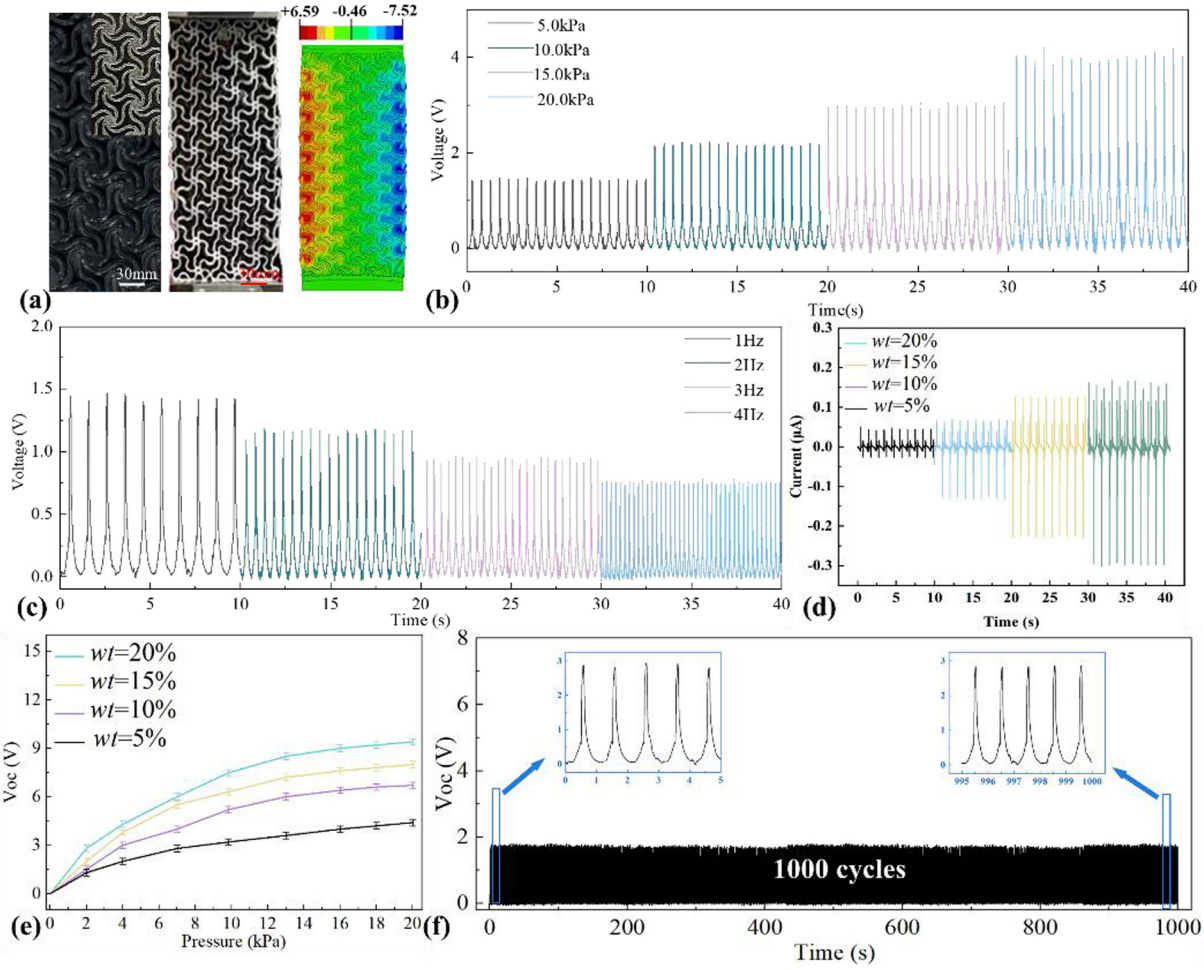

Figure 8. Electrical performance characterization of the self-sensing hierarchical hexa-chiral metamaterial: (a) optical image of the assembled periodic lattice composed of hierarchical hexa-chiral unit cells, together with the corresponding tensile deformation contour. The macroscopic periodic pattern represents the arrayed assembly of unit cells, while structural hierarchy is embedded within the ligament architecture of each unit cell, (b) pressure-sensing characteristics under varying applied pressure levels, (c) Output current under a uniformly applied sinusoidal pressure load, (d) frequency-dependent response signals of the sensor, (e) gradient-pressure response signals demonstrating signal stability and repeatability, and (f) loading–unloading cyclic durability test evaluating long-term operational stability.

signals was realized using this device, as shown in Figure 9(d). The test results indicated that the sensor has high acquisition quality for the same tester, manifested by stable peak values, a consistent number of inflection points, and high cycle similarity. This test result demonstrated that the self-sensing metamaterial can stably and accurately collect human pulse signals. The negative Poisson's ratio substrate induces lateral expansion under axial stretching, which enhances in-plane strain redistribution and contributes to the effective electromechanical coupling during deformation.

Conclusions

This work presents the design, analytical modeling, fabrication, and experimental characterization of a hierarchical hexa-chiral mechanical metamaterial integrated with a flexible piezoelectric composite sensor. An analytical framework based on Euler–Bernoulli beam mechanics and Castigliano's theorem was developed to predict the effective elastic modulus and Poisson's ratio of both first- and second-order structures, with predictions validated against finite-element simulations to within 8%–11%.The metamaterial exhibits biomimetic J-shaped stress–strain behavior and a negative Poisson's ratio (ν ranging from approximately -1.0 to 0), both confirmed by FEA and mechanical testing. A multilayer flexible sensor was then fabricated by integrating the printed PLA skeleton with a piezoelectric composite film of P(VDF-TrFE) and $BaTiO_3$ dispersed in an Ecoflex matrix, encapsulated in PDMS. The sensor achieves a gage factor of 2432.85, a pressure sensitivity of 3 kPa^{-1}, and stable output over 10,000 cycles, and was demonstrated for detection of finger

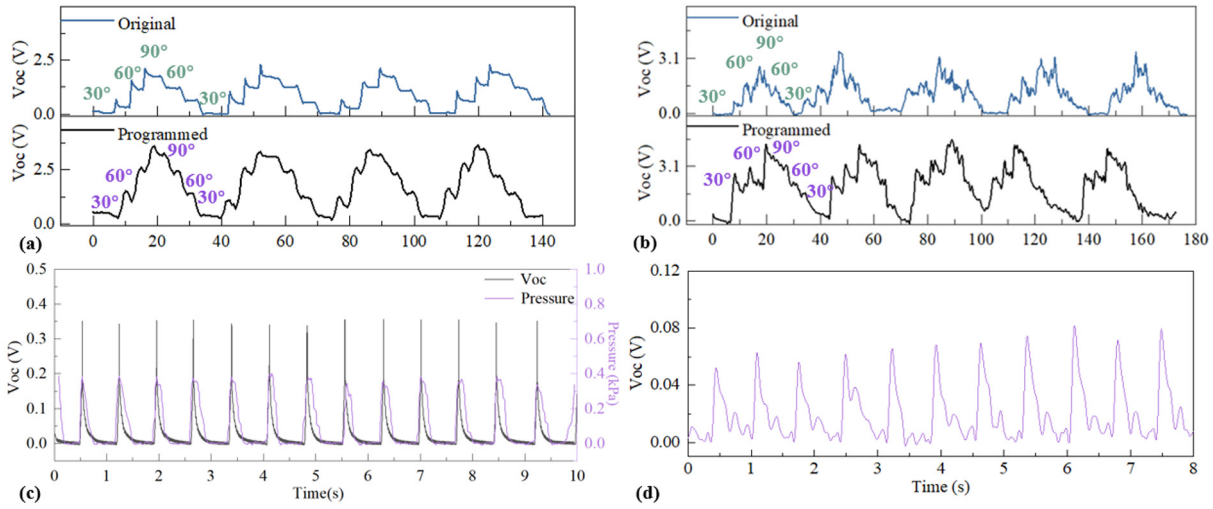

Figure 9. Application of the self-sensing metamaterials. Real-time motion monitoring of (a) wrist and (b) finger under different bending angles with a flexible metamaterial sensor, (c) the real-time output response to the drops, and (d) pulse signal detection results.

motion, wrist bending, and radial artery pulse signals. Owing to the thermally activated shape-memory effect of the PLA skeleton ($Tg \approx 60°C$), the device can be reprogrammeded into a deformed configuration that shifts the substrate stiffness and thereby adjusts the sensing sensitivity, enabling post-fabrication tuning without component replacement. These results demonstrate that a geometrically tunable chiral metamaterial substrate combined with flexible piezoelectric sensing and shape-memory programming offers a practical route to reconfigurable mechanical sensing for wearable monitoring applications.

ORCID iD

Nan Li https://orcid.org/0000-0001-6164-5185

Funding

The authors disclosed receipt of the following financial support for the research, authorship, and/or publication of this article: This work was financially supported by the Postdoctoral Fellowship Program of China Postdoctoral Science Foundation (Grant No. GZC20252753), China Postdoctoral Science Foundation (Grant No. 2025M784349), Heilongjiang Postdoctoral Fund (No, LBH-Z25143), Natural Science Foundation of Heilongjiang Province of China (QC2025005), the open research fund of Suzhou Laboratory (No.SZLAB-1508-2024-ZD016), the open research fund of State Key Laboratory of Mechanics and Control for Aerospace Structures (Grant No.MCAS-E-0125K01).

Declaration of conflicting interests

The authors declared no potential conflicts of interest with respect to the research, authorship, and/or publication of this article.

Data availability statement

The data that support the findings of this study are available from the corresponding author upon reasonable request.

References

Benight SJ, Wang C, Tok JBH, et al. (2013) Stretchable and self-healing polymers and devices for electronic skin. *Progress in Polymer Science* 38(12): 1961–1977.

Chou HH, Nguyen A, Chortos A, et al. (2015) A chameleon-inspired stretchable electronic skin with interactive colour changing controlled by tactile sensing. *Nature Communications* 6(1): 8011.

Fang H, Li S, Thota M, et al. (2019) Origami lattices and folding-induced lattice transformations. *Physical Review Research* 1(2): 023010.

Feng F, Dang X, James RD, et al. (2020) The designs and deformations of rigidly and flat-foldable quadrilateral mesh origami. *Journal of the Mechanics and Physics of Solids* 142: 104018.

Hong J, Shin JM, Kim GM, et al. (2017) 9.1-inch stretchable AMOLED display based on LTPS technology. *Journal of the Society for Information Display* 25(3): 194–199.

Huang HH, Wong BL and Chou YC (2016) Design and properties of 3D-printed chiral auxetic metamaterials by reconfigurable connections. *Physica Status Solidi (B)* 253(8): 1557–1564.

Huang Y, Zhu C, Xiong W, et al. (2022) Flexible smart sensing skin for "Fly-by-Feel" morphing aircraft. *Science China Technological Sciences* 65(1): 1–29.

Jeong SH, Hagman A, Hjort K, et al. (2012) Liquid alloy printing of microfluidic stretchable electronics. *Lab on A Chip* 12(22): 4657–4664.

Kai H, Suda W, Ogawa Y, et al. (2017) Intrinsically stretchable electrochromic display by a composite film of poly(3,4-ethylenedioxythiophene) and polyurethane. *ACS Applied Materials & Interfaces* 9(23): 19513–19518.

Li J, Liang Z, Li T, et al. (2025) A comprehensive review on 4D printing and applications of thermo-induced shape

memory polymers. *International Journal of Smart and Nano Materials* 16(1): 24–83.
Li N, Liu L, Liu Y, et al. (2024) Metamaterial-based electronic skin with conformality and multisensory integration. *Advanced Functional Materials* 34(49): 2406789.
Lin Q, Huang H, Jing Y, et al. (2014) Flexible photovoltaic technologies. *Journal of Materials Chemistry C* 2(7): 1233–1247.
Li N, Zhao W, Li F, et al. (2023) A 4D-printed programmable soft network with fractal design and adjustable hydrophobic performance. *Matters* 6(3): 940–962.
Lu N and Kim DH (2014) Flexible and stretchable electronics paving the way for soft robotics. *Soft Robotics* 1(1): 53–62.
Majidi C (2019) Soft-matter engineering for soft robotics. *Advanced Materials Technologies* 4(2): 1800477.
Markvicka EJ, Bartlett MD, Huang X, et al. (2018) An autonomously electrically self-healing liquid metal-elastomer composite for robust soft-matter robotics and electronics. *Nature Materials* 17(7): 618–624.
Meza LR, Zelhofer AJ, Clarke N, et al. (2015) Resilient 3D hierarchical architected metamaterials. *Proceedings of the National Academy of Sciences* 112(37): 11502–11507.
Overvelde JT, de Jong TA, Shevchenko Y, et al. (2016) A three-dimensional actuated origami-inspired transformable metamaterial with multiple degrees of freedom. *Nature Communications* 7(1): 10929.
Rogers JA, Someya T and Huang Y (2010) Materials and mechanics for stretchable electronics. *Science* 327(5973): 1603–1607.
Sekitani T and Someya T (2012) Stretchable organic integrated circuits for large-area electronic skin surfaces. *MRS Bulletin* 37(3): 236–245.
Song Y, Min J and Gao W (2019) Wearable and implantable electronics: Moving toward precision therapy. *ACS Nano* 13(11): 12280–12286.
Su Y, Liu Z and Xu L (2016) Organ-mounted electronics: An universal and easy-to-use model for the pressure of arbitrary-shape 3D multifunctional integumentary cardiac membranes. *Advanced Healthcare Materials* 5(8): 866.
Wang D, Dong L and Gu G (2023) 3D printed fractal metamaterials with tunable mechanical properties and shape reconfiguration. *Advanced Functional Materials* 33(1): 2208849.
Wang K, Chang YH, Chen Y, et al. (2015a) Designable dual-material auxetic metamaterials using three-dimensional printing. *Materials & Design* 67: 159–164.
Wang X, Dong L, Zhang H, et al. (2015b) Recent progress in electronic skin. *Advanced Science* 2(10): 1500169.
Xu L, Gutbrod SR, Ma Y, et al. (2015) Materials and fractal designs for 3D multifunctional integumentary membranes with capabilities in cardiac electrotherapy. *Advanced Materials* 27(10): 1731–1737.
Zhai Z, Wu L and Jiang H (2021) Mechanical metamaterials based on origami and kirigami. *Applied Physics Reviews* 8(4): 041219.
Zhao Y, Wu J, Shen P, et al. (2025) A review of wearable flexible sensors for sports: From materials to applications. *International Journal of Smart and Nano Materials* 16(4): 695–725.

Appendix 1

$$[\overline{T}^{(1)}] = \begin{pmatrix} \frac{1}{64}[\csc^3\frac{\theta}{2}(\theta + \sin\theta) - 8\cos\frac{\theta}{2} + 2\cos\frac{\theta}{2}\cot\frac{\theta}{2}] & \frac{1}{32}(-\theta\cos\frac{\theta}{2} + 2\csc\frac{\theta}{2}) & \frac{1}{32}(\theta\cos\frac{\theta}{2} - 2\csc\frac{\theta}{2}) \\ \frac{1}{32}(-\theta\cos\frac{\theta}{2} + 2\csc\frac{\theta}{2}) & \frac{\csc\frac{\theta}{2}}{64}(\theta\csc^2\frac{\theta}{2} - \csc\frac{\theta}{2} + 10\theta) & \frac{\csc\frac{\theta}{2}}{64}(-\theta\csc^2\frac{\theta}{2} + \csc\frac{\theta}{2} + 6\theta) \\ \frac{1}{32}(\theta\cos\frac{\theta}{2} - 2\csc\frac{\theta}{2}) & \frac{\csc\frac{\theta}{2}}{64}(-\theta\csc^2\frac{\theta}{2} + \csc\frac{\theta}{2} + 6\theta) & \frac{1}{64}\csc\frac{\theta}{2}(\theta\csc^2\frac{\theta}{2} - \csc\frac{\theta}{2} + 10\theta) \end{pmatrix}$$

Appendix 2

$$C_k = \begin{pmatrix} \frac{\cos\gamma_1}{G} & -\frac{\cos\gamma_1}{4G\sin\gamma_3} & \frac{\cos\gamma_1}{4G\sin\gamma_3} \\ -2\sin\gamma_2\sin\gamma_8 + 2\sin\gamma_4\sin\gamma_1 & 1 + \frac{-\cos\gamma_1\sin\gamma_4 + \sin\gamma_8\cos\gamma_2}{2\sin\gamma_3} & \frac{\cos\gamma_1\sin\gamma_4 - \sin\gamma_8\cos\gamma_2}{2\sin\gamma_3} \\ -2\sin\gamma_2\sin\gamma_8 & 1 + \frac{\sin\gamma_8\cos\gamma_2}{2\sin\gamma_3} & -\frac{\sin\gamma_8\cos\gamma_2}{2\sin\gamma_3} \end{pmatrix} \quad (21)$$

When $n + 1 \leqslant k \leqslant 2n$,

$$C_k = \begin{pmatrix} \frac{\cos\gamma_5}{G} & \frac{-\sin\gamma_5}{4G\sin\gamma_3} & \frac{\sin\gamma_5}{4G\sin\gamma_3} \\ -2\sin\gamma_6\sin\gamma_7 & -\frac{\sin\gamma_6\cos\gamma_7}{2\sin\gamma_3} & 1 + \frac{\sin\gamma_6\cos\gamma_7}{2\sin\gamma_3} \\ 2\sin\gamma_5\sin\gamma_4 - 2\sin\gamma_6\sin_7 & \frac{\cos\gamma_5\sin\gamma_4 - \sin\gamma_6\cos\gamma_7}{2\sin\gamma_3} & 1 + \frac{-\cos\gamma_5\sin\gamma_4 + \cos\gamma_7\sin\gamma_6}{2\sin\gamma_3} \end{pmatrix} \quad (22)$$

$$[D] = \begin{pmatrix} c_{11}^2 & c_{21}^2 & c_{31}^2 & 2c_{11}c_{21} & 2c_{11}c_{31} & 2c_{21}c_{31} \\ c_{12}^2 & c_{22}^2 & c_{32}^2 & 2c_{12}c_{22} & 2c_{12}c_{32} & 2c_{32}c_{22} \\ c_{13}^2 & c_{23}^2 & c_{33}^2 & 2c_{13}c_{23} & 2c_{13}c_{33} & 2c_{23}c_{33} \\ c_{11}c_{12} & c_{12}c_{21} & c_{31}c_{32} & c_{21}(c_{12} + c_{22}) & c_{12}c_{31} + c_{11}c_{32} & c_{22}c_{31} + c_{21}c_{32} \\ c_{11}c_{13} & c_{21}c_{23} & c_{31}c_{33} & c_{21}c_{31} + c_{11}c_{23} & c_{13}c_{31} + c_{11}c_{33} & c_{23}c_{31} + c_{21}c_{33} \\ c_{12}c_{13} & c_{22}c_{23} & c_{32}c_{33} & c_{13}c_{22} + c_{12}c_{23} & c_{13}c_{31} + c_{12}c_{33} & c_{22}c_{32} + c_{23}^2 \end{pmatrix} \quad (23)$$

Appendix 3

$$\sqrt{3}\bar{N}_3 + \sqrt{3}\bar{N}_2 + (\bar{M}_{3A} - \bar{M}_{3B}) - (\bar{M}_{2A} - \bar{M}_{2B}) = 0$$
$$2(\bar{M}_{1A} - \bar{M}_{1B}) + (\bar{M}_{2A} - \bar{M}_{2B}) - \sqrt{3}\bar{N}_2 = 0$$
$$\sigma_x = \frac{4\bar{N}_1 + \bar{N}_2 + \bar{N}_3 - \sqrt{3}(\bar{M}_{3A} - \bar{M}_{3B}) + \sqrt{3}(\bar{M}_{2A} - \bar{M}_{2B})}{2\sqrt{3}A\bar{w}\left(\frac{L_0^2}{E_S I}\right)} \tag{24}$$

$$(\bar{M}_{1A} - \bar{M}_{1B}) + (\bar{M}_{2A} - \bar{M}_{2B}) + (\bar{M}_{3A} - \bar{M}_{3B}) = 0 \tag{25}$$

$$\begin{cases} \phi_1 - \gamma_{3A} + \gamma_{2B} = \dfrac{\pi}{3} + \theta_B - \theta_A \\ \phi_2 - \gamma_{1A} + \gamma_{3B} = \dfrac{\pi}{3} + \theta_B - \theta_A \\ \phi_3 - \gamma_{2A} + \gamma_{1B} = \dfrac{\pi}{3} + \theta_B - \theta_A \end{cases}$$

$$\frac{L_1}{\sin\phi_1} = \frac{L_2}{\sin\phi_2} = \frac{L_3}{\sin\phi_3}, \quad \text{and} \quad \sum_{i=1}^{3} \phi_i = \pi \tag{26}$$

$$\bar{u}_2 - \bar{u}_1 = \frac{1}{\sqrt{3}}(\omega_{3A} + \omega_{2B} - \omega_{1A} - \omega_{3B}),$$
$$\bar{u}_3 - \bar{u}_1 = \frac{1}{\sqrt{3}}(\omega_{3A} + \omega_{2B} - \omega_{2A} - \omega_{1B})$$
$$\omega_{1A} + \omega_{2A} + \omega_{3A} + \omega_{1B} + \omega_{2B} + \omega_{3B} = 0 \tag{27}$$

$$\bar{u}_2 - \bar{u}_1 = \frac{1}{\sqrt{3}}(\omega_{1B} + \omega_{3A} - \omega_{2A} - \omega_{3B}), \tag{28}$$
$$\bar{u}_3 - \bar{u}_1 = \frac{1}{\sqrt{3}}(\omega_{2B} + \omega_{1A} - \omega_{2A} - \omega_{3B})$$

$$\varepsilon_x = \bar{u}_1 \tag{29}$$